



2 DOCTORAL THESIS

---

4 Optimisation studies and background  
5 estimation in searches for the supersymmetric  
6 partner of the top quark in all-hadronic final  
7 states with the ATLAS Detector at the LHC

---

9 *A thesis submitted in fulfillment of the requirements  
10 for the degree of Doctor of Philosophy*

11 *in the*

12 Experimental Particle Physics Research Group  
13 School of Mathematical and Physical Sciences

14 *Author:*  
15 Fabrizio MIANO

*Supervisor:*  
Dr. Fabrizio SALVATORE

13th October 2017

*Dedicated to my family.*

*Have no fear for atomic energy  
'cause none of them can stop the  
time*

17

---

Robert Nesta Marley

18

## *Acknowledgments*

<sup>19</sup> Thanks to every single thing that went wrong. It made me stronger.

## *Declaration*

21 I, Fabrizio MIANO, hereby declare that this thesis, titled, "Optimisation studies and back-  
22 ground estimation in searches for the supersymmetric partner of the top quark in all-  
23 hadronic final states with the ATLAS Detector at the LHC" has not been and will not be,  
24 submitted in whole or in part to another University for the award of any other degree.

25 *Brighton, June 2018*

27                                  University of Sussex  
28                                  School of Mathematical and Physical Sciences  
29                                  Experimental Particle Physics Research Group

30                                  Doctoral Thesis

31                                  \_\_\_\_\_  
32                                  Optimisation studies and background estimation in searches for  
33                                  the supersymmetric partner of the top quark in all-hadronic final  
34                                  states with the ATLAS Detector at the LHC  
35                                  \_\_\_\_\_

36                                  by Fabrizio MIANO

37                                  *Abstract*

38     This thesis presents searches for supersymmetry in  $\sqrt{s} = 13$  TeV proton-proton collisions  
39     at the LHC using data collected by the ATLAS detector in 2015, 2016 and 2017. Events  
40     with 4 or more jets and missing transverse energy were selected. Kinematic variables  
41     were investigated and optimisations were performed to increase the sensitivity to su-  
42     persymmetric signals. Standard Model backgrounds were estimated by means of Monte  
43     Carlo simulations and data-driven techniques. Before analysing the data in the blinded  
44     signal regions the agreement between data and background predictions and the extrapola-  
45     tions from control and validation regions to signal regions were validated. The analysis  
46     yielded no significant excess in any of the analyses performed. Therefore limits were  
47     set and the results were interpreted as lower bounds on the masses of supersymmetric  
48     particles in various scenarios and models.

# 49 Contents

50	<b>Introduction</b>	1
51	<b>1 The Standard Model, Supersymmetry, and the motivations behind it</b>	2
52	1.1 The Standard Model . . . . .	2
53	1.1.1 Overview . . . . .	3
54	1.1.2 Limitations of the Standard Model . . . . .	6
55	1.2 Supersymmetry . . . . .	6
56	1.2.1 Why SUSY? . . . . .	6
57	1.2.2 Minimal Supersymmetric Standard Model . . . . .	6
58	1.2.3 $R$ -parity SUSY . . . . .	6
59	1.2.4 Simplified models . . . . .	7
60	1.2.5 Phenomenological MSSM . . . . .	7
61	<b>2 The ATLAS Experiment at the LHC</b>	8
62	2.1 The LHC . . . . .	8
63	2.2 The ATLAS Detector . . . . .	10
64	2.2.1 The Magnet System . . . . .	12
65	2.2.2 The Inner Detector . . . . .	13
66	2.2.3 The Calorimeters . . . . .	16
67	2.2.4 The Muon Spectrometer . . . . .	17
68	2.3 The ATLAS Trigger System . . . . .	19
69	2.3.1 Level 1 Trigger . . . . .	20
70	2.3.2 High-Level Trigger . . . . .	20
71	<b>3 The <math>b</math>-jet Trigger Signature in ATLAS</b>	22
72	3.1 Trigger Efficiency . . . . .	22

73	<b>4 Event Simulation and Reconstruction</b>	23
74	<b>4.1 Event Generation</b> . . . . .	23
75	<b>4.1.1 Parton Distribution Functions (PDFs)</b> . . . . .	23
76	<b>4.1.2 Matrix Element Calculation</b> . . . . .	23
77	<b>4.1.3 Parton Showers</b> . . . . .	23
78	<b>4.1.4 Hadronisation</b> . . . . .	23
79	<b>4.2 Detector Simulation</b> . . . . .	23
80	<b>5 Stop searches in final states with jets and missing transverse energy</b>	24
81	<b>6 Results and Statistical Interpretations</b>	25
82	<b>Trigger</b>	26
83	<b>Bibliography</b>	27

# <sup>84</sup> List of Tables

<sup>85</sup>	1.1 Forces and mediators described by the SM . . . . .	4
---------------	--------------------------------------------------------	---

<sup>86</sup> **List of Figures**

<sup>87</sup> 2.1	CERN Accelerator complex. The LHC is the last ring (dark grey line). Smaller machines are used for early-stage acceleration and also to provide beams for other experiments [1]. . . . .	10
<sup>90</sup> 2.2	Cut-away view of the ATLAS detector. The dimensions of the detector are 25 m in height and 44 m in length. The overall weight of the detector is approximately 7000 tonnes [1]. . . . .	11
<sup>93</sup> 2.3	The ATLAS magnet system. . . . .	12
<sup>94</sup> 2.4	The ATLAS Inner Detector . . . . .	14
<sup>95</sup> 2.5	A computer generated image of the full calorimeter. . . . .	16
<sup>96</sup> 2.6	Cut-away view of the ATLAS muon system [2]. . . . .	18
<sup>97</sup> 2.7	The ATLAS TDAQ system. L1Topo and FTK were being commissioned during 2015 and not used for the results shown in this thesis [3]. . . . .	19

# <sup>99</sup> Introduction

<sup>100</sup> Last thing to write

<sup>101</sup> **Chapter 1**

<sup>102</sup> **The Standard Model,  
Supersymmetry, and the motivations  
behind it**

<sup>105</sup>

*A theory is something nobody believes, except the person who made it. An experiment is something everybody believes, except the person who made it.*

---

Albert Einstein

<sup>106</sup> The Standard Model (SM) of particle physics is an effective theory that aims to provide  
<sup>107</sup> a general description of fundamental particles and the phenomena we see in nature, i. e.  
<sup>108</sup> the way they interact. Unfortunately, our understanding of nature is still limited due to  
<sup>109</sup> some opened question to which the SM is not able to answer to, yet.

<sup>110</sup> In this chapter, an overview of the SM will be presented in Section 1.1 together with  
<sup>111</sup> the limitations of such theory and some of the reasons behind the need of an extension.  
<sup>112</sup> For the last decades theoretical physicsts have been trying to provide extensions to the  
<sup>113</sup> SM, the so-called beyond-the-SM theories. Among these, one of the most popular, Super-  
<sup>114</sup> symmetry which will be discussed in Section 1.2.

<sup>115</sup> **1.1 The Standard Model**

<sup>116</sup> The 20<sup>th</sup> century can be considered a quantum revolution. Several experiments led to  
<sup>117</sup> discoveries which were found to be, together with the formalised theory, a solid base of

<sup>118</sup> the Standard Model of particle physics and our description of nature. Several particles  
<sup>119</sup> were predicted first by the SM and then experimentally observed e.g. the  $W$  and the  $Z$   
<sup>120</sup> bosons, the  $\tau$  lepton, [4], and more recently the Higgs boson at the LHC discovered by  
<sup>121</sup> ATLAS [5] and CMS [6].

<sup>122</sup> The SM lays on a Quantum Field Theory (QFT) where particles are treated like fields.  
<sup>123</sup> It can describe three of the four fundamental forces; weak, electromagnetic, and strong.  
<sup>124</sup> As of today, gravity is not considered in the SM. Sections 1.1.1 and 1.1.2 will be focused  
<sup>125</sup> on the description of the fields together with the carriers of the information, and on the  
<sup>126</sup> limitations that such theory implies, respectively.

### <sup>127</sup> 1.1.1 Overview

<sup>128</sup> The most general classification of the particles within the SM can be made by means of  
<sup>129</sup> spin. Fermions have half-integer spin values - and are usually referred to as matter -, and  
<sup>130</sup> bosons have integer-spin values. A noteworthy subset of bosons is formed by the Spin-1  
<sup>131</sup> bosons (also known as gauge bosons). These can be considered the information carriers  
<sup>132</sup> or, in fact, the mediators of the forces.

### <sup>133</sup> Fermions

<sup>134</sup> Six quarks and six leptons belong to the fermions family. In particular, fermions can be  
<sup>135</sup> grouped into three generations. Each generation contains four particles; one up- and  
<sup>136</sup> one down-type quark, one charged lepton and one neutral lepton. The masses of the  
<sup>137</sup> charged leptons and quarks increase with the generation. The six quarks of the SM can  
<sup>138</sup> be grouped into three doublets:

$$\begin{pmatrix} u \\ d \end{pmatrix}, \quad \begin{pmatrix} c \\ s \end{pmatrix}, \quad \begin{pmatrix} t \\ b \end{pmatrix}$$

<sup>139</sup> The up-type quarks (up, charm, top) have charge  $+\frac{2}{3}e$  and the down-type quarks (down,  
<sup>140</sup> strange, beauty/bottom) have charge  $-\frac{1}{3}e$ , where  $e$  is the electron charge. Quarks also  
<sup>141</sup> have another quantum number that can be seen as the analogue of the electric charge,  
<sup>142</sup> which is the colour charge. This can exist in three different states; "red", "green" and  
<sup>143</sup> "blue". Moreover, as a consequence of *confinement*, which will be discussed later on in  
<sup>144</sup> this section, quarks cannot exist as free particles. They rather group to form hadronic  
<sup>145</sup> matter, also known as *hadrons*. There are two kinds of hadrons; mesons and baryons.  
<sup>146</sup> Mesons are quark-antiquark systems, e.g. the pion, and baryons are three-quark system,

<sup>147</sup> e.g. protons and neutrons. Quarks and anti-quarks have a baryon number of  $\frac{1}{3}$  and  $-\frac{1}{3}$ , respectively.

<sup>149</sup> There are six leptons and they can be classified in charged leptons (electron  $e$ , muon  $\mu$ , tau  $\tau$ ) and neutral leptons (electron neutrino  $\nu_e$ , muon neutrino  $\nu_\mu$ , tau neutrino  $\nu_\tau$ ).

$$\begin{pmatrix} \nu_e \\ e^- \end{pmatrix}, \quad \begin{pmatrix} \nu_\mu \\ \mu^- \end{pmatrix}, \quad \begin{pmatrix} \nu_\tau \\ \tau^- \end{pmatrix}$$

<sup>151</sup> Each lepton has a characteristic quantum number, called lepton number ( $L$ ). Negatively <sup>152</sup> (positively) charged leptons have  $L = -1$  ( $L = 1$ ) and neutral leptons have  $L = 0$ . The <sup>153</sup> lepton number is conserved in all the interactions.

## <sup>154</sup> Forces of Nature

<sup>155</sup> Forces in the SM are described by gauge theories, where the interactions is mediated by a <sup>156</sup> vector gauge boson. The electromagnetic force is described by Quantum ElectroDynam- <sup>157</sup> ics (QED) and, as its mediator is the photon ( $\gamma$ ) which couples to charged particles, it only <sup>158</sup> affects charged leptons and quarks, whereas neutrinos cannot. They are instead affected <sup>159</sup> by the weak force which is mediated by the bosons  $W^\pm$  and  $Z^0$ . The weak interaction is <sup>160</sup> associated with handedness (the projection of a particle spin onto its direction of motion). <sup>161</sup> Both leptons and quarks have left- and right-handed components. However, only the <sup>162</sup> left-handed (right-handed) component for neutrinos (anti-neutrinos) has been observed. <sup>163</sup> This means that nature prefers to produce left-handed neutrinos and right-handed anti- <sup>164</sup> neutrinos, which is the so-called parity violation. The strong interactions, mediated by <sup>165</sup> the gluon (electrically neutral and massless), is described by Quantum ChromoDynamics <sup>166</sup> (QCD). Table 1.1 summarises the forces described in the SM and their mediators' main <sup>167</sup> characteristics. Finally, the gravitational force, which is believed to be mediated by the <sup>168</sup> graviton, is not included in Table 1.1 as it is not part of the SM.

Table 1.1: Forces and mediators described by the SM

Force	Name	Symbol	Mass [GeV]	Charge
Electromagnetic	Photon	$\gamma$	0	0
Weak	W	$W^\pm$	80.398	$\pm e$
	Z	$Z^0$	91.188	0
Strong	Gluon	$g$	0	0

<sup>169</sup> **Symmetries and Gauge Groups**

<sup>170</sup> In 1915, the mathematician Emmy Noether (23 March 1882 – 14 April 1935) proved that  
<sup>171</sup> every differentiable symmetry of the action - defined as the integral over space of a Lag-  
<sup>172</sup> rangian density function - of a physical system has a corresponding conservation law.  
<sup>173</sup> More generally, a symmetry is a property of a physical system. Under certain transform-  
<sup>174</sup> ations this property is preserved.

<sup>175</sup> A gauge theory in QFT, is a theory in which the Lagrangian is invariant under a  
<sup>176</sup> continuous group of local transformation. Group theory was then adopted to describe  
<sup>177</sup> the symmetries conserved in the SM. The gauge group of the theory is the *Lie Group*.  
<sup>178</sup> It contains all the transformations between possible gauges. The Lie algebra of group  
<sup>179</sup> generators is therefore associated with any Lie group and for each group generator there  
<sup>180</sup> emerges a corresponding field: the gauge field. The quanta of the gauge fields are called  
<sup>181</sup> *gauge bosons*.

<sup>182</sup> The three SM interactions can therefore be mathematically described by the following:

$$U(1)_Y \times SU(2)_L \times SU(3)_C \quad (1.1)$$

<sup>183</sup> Here,  $Y$  is the weak hypercharge, used to estimate the correlation between the electric  
<sup>184</sup> charge ( $Q$ ) and the third component of the weak isospin ( $I_3$ ) via the relation  $Q = I_3 + Y/2$ ,  
<sup>185</sup> where  $I_3$  can either be  $\pm 1/2$  or 0 for left-handed and right-handed particles, respectively;  
<sup>186</sup>  $C$  the colour charge and  $L$  the left-handedness.

<sup>187</sup> As of today, we can describe three of the four forces of nature with group theory. QED  
<sup>188</sup> is an Abelian gauge theory with  $U(1)$  as symmetry group, with the electromagnetic four-  
<sup>189</sup> potential as its gauge field and with the photon as its gauge boson [7]. The interactions  
<sup>190</sup> between charged fermions occurs by the exchange of a massless photon.

<sup>191</sup> The weak interaction and the strong interactions are non-Abelian gauge theories with  
<sup>192</sup> gauge groups  $SU(2)$  and  $SU(3)$ , respectively. As a consequence of being non-Abelian  
<sup>193</sup> the generators commutators are non-vanishing and therefore the gauge bosons can self-  
<sup>194</sup> interact. The  $SU(2)$  generators of the weak interaction are the massless gauge bosons  
<sup>195</sup>  $W_\mu^{\alpha=1,\dots,3}$  and, as mentioned earlier on in this chapter, they violate the parity by acting  
<sup>196</sup> only on left-handed particles.

<sup>197</sup> The gauge bosons of  $SU(3)_C$  are eight massless gluons,  $G_\mu^{\alpha=1,\dots,8}$ . The strong interac-  
<sup>198</sup> tion does not distinguish left- and right-handed particles.

<sup>199</sup> In 1979 Sheldon Glashow, Abdus Salam, and Steven Weinberg were awarded the No-  
<sup>200</sup> bel Prize in Physics for their contributions to the so-called electroweak unification. Weak

and electromagnetic interactions were unified. In the mathematical description of the SM in 1.1 the electroweak interaction is described by  $U(1)_Y \times SU(2)_L$ . Here, the gauge field associated with  $U(1)_Y$  is the massless  $B_\mu^0$ . The electroweak physical bosons  $W$ ,  $Z$  and  $\gamma$  are related to the four unphysical bosons  $W_\mu^{\alpha=1,\dots,3}$  and  $B_\mu^0$ . In particular, the field mixing of gauge bosons that gives birth to the physical ones can be mathematically expressed by the following:

$$W_\mu^\pm = \frac{1}{\sqrt{2}} (W_\mu^1 \mp i W_\mu^2) \quad (1.2)$$

207

$$Z_\mu = B_\mu^0 \cos(\theta_W) + W_\mu^3 \sin(\theta_W) \quad (1.3)$$

208

$$A_\mu = -B_\mu^0 \sin(\theta_W) + W_\mu^3 \cos(\theta_W) \quad (1.4)$$

Here,  $\theta_W$  is the so-called *Weinberg angle* which is the angle by which spontaneous symmetry breaking rotates the original  $W_\mu^3$  and  $B_\mu^0$ , producing the physical  $Z$ , and the photon. It can be experimentally determined as the ratio of the electroweak coupling constants  $g$  and  $g'$  using the relation  $\tan(\theta_W) = g/g'$ . Finally, the Quarks that interact through weak interaction are mixtures of SM eigenstates as described by the CKM matrix [8].

## 215 Electroweak Symmetry Breaking and the Higgs mechanism

### 216 1.1.2 Limitations of the Standard Model

217 bla

## 218 1.2 Supersymmetry

### 219 1.2.1 Why SUSY?

220 bla

### 221 1.2.2 Minimal Supersymmetric Standard Model

222 bla

### 223 1.2.3 R-parity SUSY

224 bla

---

**225 1.2.4 Simplified models**

226 bla

**227 1.2.5 Phenomenological MSSM**

228 bla

<sup>229</sup> **Chapter 2**

<sup>230</sup> **The ATLAS Experiment at the LHC**

<sup>231</sup> ATLAS (A Toroidal LHC ApparatuS) is one of the four main experiments (ATLAS, CMS,  
<sup>232</sup> ALICE, LHCb) taking data at a center-of-mass energy of 13 TeV using beams delivered by  
<sup>233</sup> the Large Hadron Collider (LHC). In this chapter an overview of the LHC will be given  
<sup>234</sup> in Section 2.1, then the ATLAS detector will be described in Section 2.2, and finally the  
<sup>235</sup> Trigger system, used to cleverly store the data, will be described in Section 2.3. A more  
<sup>236</sup> in-depth description of the Trigger algorithms I have been involved in will be given in  
<sup>237</sup> Chapter 3.

<sup>238</sup> **2.1 The LHC**

<sup>239</sup> As of today, the LHC is the world's largest and most powerful particle accelerator. It  
<sup>240</sup> was designed to help answer some of the fundamental open questions in particle phys-  
<sup>241</sup> ics by colliding protons at an unprecedented energy and luminosity. It is located at the  
<sup>242</sup> European Organisation for Nuclear Research (CERN), in the Geneva area, at a depth ran-  
<sup>243</sup> ging from 50 to 175 metres underground. It consists of a 27-kilometre ring made of su-  
<sup>244</sup> perconducting magnets, and inside it two high-energy particle beams travel in opposite  
<sup>245</sup> directions and in separate beam pipes.

<sup>246</sup> The beams are guided around the ring by a strong magnetic field generated by coils -  
<sup>247</sup> made of special electric cables - that can operate in a superconducting regime. 1232 super-  
<sup>248</sup> conducting dipole and 392 quadrupole magnets, with an average magnetic field of 8.3 T,  
<sup>249</sup> are employed and kept at a temperature below 1.7 K, in order to preserve their supercon-  
<sup>250</sup> ducting properties. The formers are used to bend the beams and the latters to keep them  
<sup>251</sup> focused while they get accelerated.

<sup>252</sup> The collider first went live on September 2008 even though, due to a magnet quench

253 incident that damaged over 50 superconducting magnets, it has been operational since  
 254 November 2009 when low-energy beams circulated in the tunnel for the first time since  
 255 the incident. This also marked the start of the main research programme and the begin-  
 256 ning of the so-called Run 1: first operational run (2009 - 2013).

## 257 Performance of the LHC

258 In June 2015 the LHC restarted delivering physics data, after a two-year break, the so-  
 259 called Long Shutdown 1 (LS1), during which the magnets were upgraded to handle the  
 260 current required to circulate 7-TeV beams. It was the beginning of the so-called Run 2 -  
 261 second operational run (2015-2018) - during which LHC has collided up to  $10^{11}$  bunches  
 262 of protons every 25 ns at the design luminosity - the highest luminosity the detector was  
 263 designed to cope with - of  $2 \cdot 10^{34} \text{ cm}^{-2} \text{s}^{-1}$ . The definition of the luminosity is:

$$\mathcal{L} = f \frac{n_b N_1 N_2}{4\pi\sigma_x\sigma_y} \quad (2.1)$$

264 where  $N_1$  and  $N_2$  are the number of protons per bunch in each of the colliding beams,  $f$   
 265 is the revolution frequency of the bunch collisions,  $n_b$  the number of proton per bunch,  
 266 and  $\sigma_x$  and  $\sigma_y$  are the horizontal and vertical dimensions of the beam. The luminosity is  
 267 strictly related to the number of collisions occurring during a certain experiment via the  
 268 following:

$$\mathcal{N}_{\text{event}} = \mathcal{L}\sigma_{\text{event}} \quad (2.2)$$

269 where  $\sigma_{\text{event}}$  is the cross section of the process under investigation. It has not only collided  
 270 protons but also heavy ions, in particular lead nuclei at  $\sqrt{s_{NN}} = 5.02 \text{ TeV}$ , at a luminosity  
 271 of  $10^{27} \text{ cm}^{-2} \text{s}^{-1}$  [9].

## 272 Acceleration stages

273 Before reaching the maximum energy, the proton beams are accelerated by smaller ac-  
 274 celerators through various stages. Figure 2.1 shows a sketch of the CERN's accelerator  
 275 complex. It all begins at the linear accelerator LINAC 2. Here protons are accelerated up  
 276 to 50 MeV, and then injected in the Proton Synchrotron Booster (PSB) where they reach  
 277 1.4 GeV. The next stage is the Proton Synchrotron (PS), which boosts the beams up to 25  
 278 GeV and then the Super Proton Synchrotron (SPS) makes them reach energies up to 450  
 279 GeV. Eventually, the beams are injected in bunches with a 25 ns spacing into the LHC,  
 280 where they travel in opposite directions, while they are accelerated to up to 13 TeV. Once

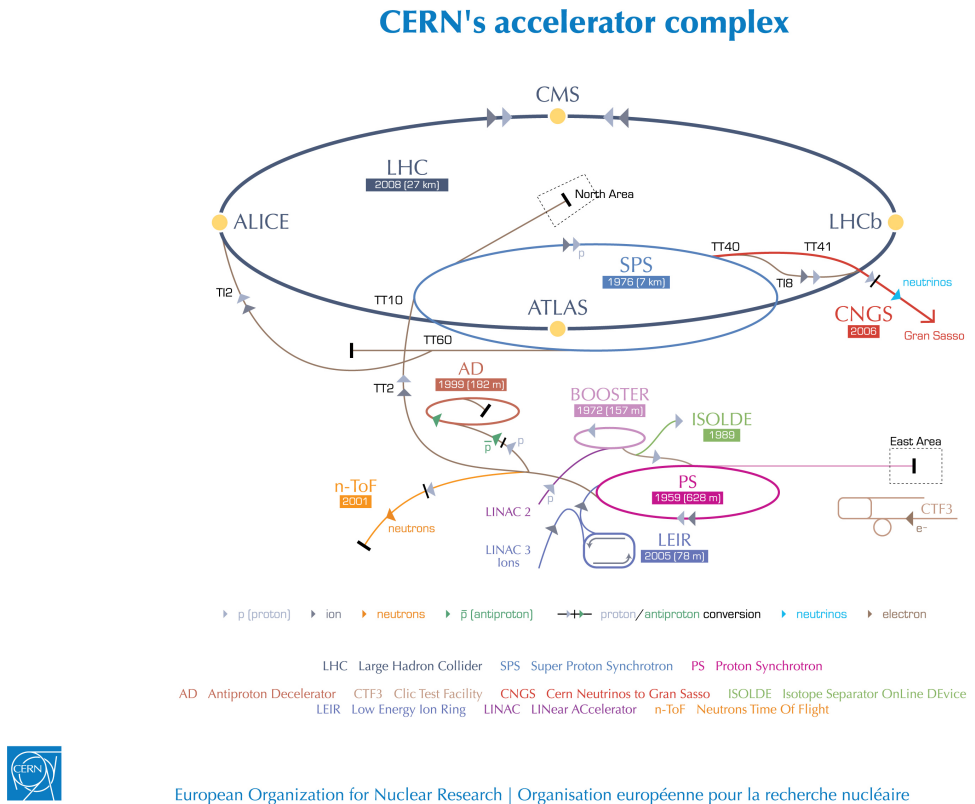


Figure 2.1: CERN Accelerator complex. The LHC is the last ring (dark grey line). Smaller machines are used for early-stage acceleration and also to provide beams for other experiments [1].

281 the bunches reach the maximum energy, they are made collide at four different points,  
282 inside four experiments around the ring [10].

283 The heavy ion beams acceleration procedure is slightly different. Their journey starts  
284 at LINAC 3 first, and the Low Energy Ion Ring (LEIR) then, before they make their way  
285 into the PS where they follow the same path as the protons [10].

286 The four large detectors on the collision points are; the multi-purpose detectors A Tor-  
287 oidal LHC ApparatuS (ATLAS), and Compact Muon Solenoid (CMS) [11], Large Hadron  
288 Collider beauty (LHCb) [12], which focuses on flavour physics, and A Large Ion Collider  
289 Experiment (ALICE) [13] which specialises in heavy ion physics. The *big four* are not the  
290 only experiments at the CERN's accelerator complex. There also are smaller experiments  
291 based at the the four caverns about the collision points e.g. TOTEM, LHCf and MoEDAL,  
292 but this will not be discussed any further in this thesis.

## 293 2.2 The ATLAS Detector

294 ATLAS is a general-purpose detector designed to collect data with the highest luminosity  
295 provided by the LHC. It is located at CERN's Point 1 cavern and it measures about 45 m in

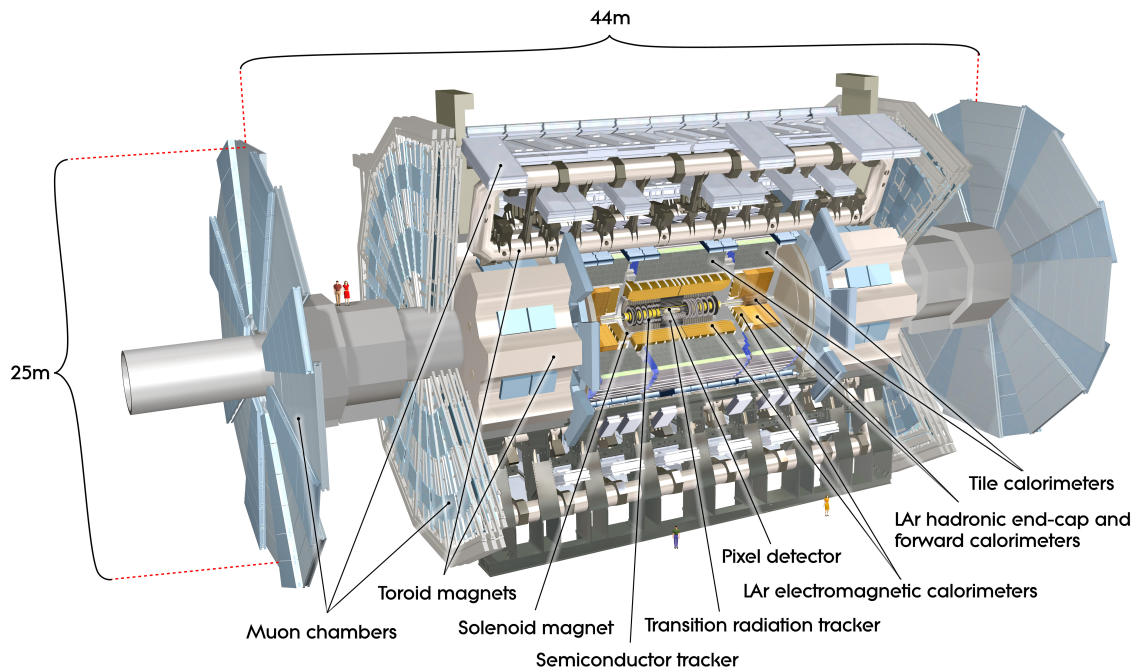


Figure 2.2: Cut-away view of the ATLAS detector. The dimensions of the detector are 25 m in height and 44 m in length. The overall weight of the detector is approximately 7000 tonnes [1].

length and 25 m in diameter. It has a forward-backward symmetric cylindrical geometry with respect to the interaction point and it is designed to reconstruct and measure physics objects such as electrons, muons, photons and hadronic jets. Its design was optimised to be as sensitive as possible to the discovery of the Higgs boson and beyond-the-Standard-Model (BSM) physics. In fact, thanks to the other sub-systems, ATLAS is able to observe all possible decay products by covering nearly  $4\pi$  steradians of solid angle.

In Figure 2.2 a cut-away view of ATLAS with all its components is shown. The inner-most layer is the Inner Detector (ID) which is the core of the tracking system and consists of a Pixel, a Silicon micro-strip tracker (SCT), and a Transition Radiation Tracker (TRT). It is submerged in a 2 T magnetic field, generated by a thin superconducting solenoid, which bends all the charged particles' trajectories allowing transverse momentum measurement. The electromagnetic and hadronic calorimeters form the next layer and they are both used to perform precise energy measurements of photons, electrons, and hadronic jets. Finally, the outermost layer corresponds to the Muon Spectrometer (MS) which, together with the ID, enclosed in a toroidal magnetic field, allows precise measurement of momentum and position of muons. These sub-detectors will be discussed in more detail in the following sections.

313 **The ATLAS coordinate system**

314 A coordinate system is taken on for the spatial definition of the sub-systems and kin-  
315 ematic measurement of physics processes. Such system is defined starting from the in-  
316 teraction point, defined as the origin. The  $z$ -axis is defined by the beam direction and the  
317  $x - y$  plan, as transverse to the beam direction.

318 A quantity, known as pseudorapidity, ( $\eta$ ), is defined to describe the angle of a particle  
319 coming out of the collision, with respect to the beam axis:

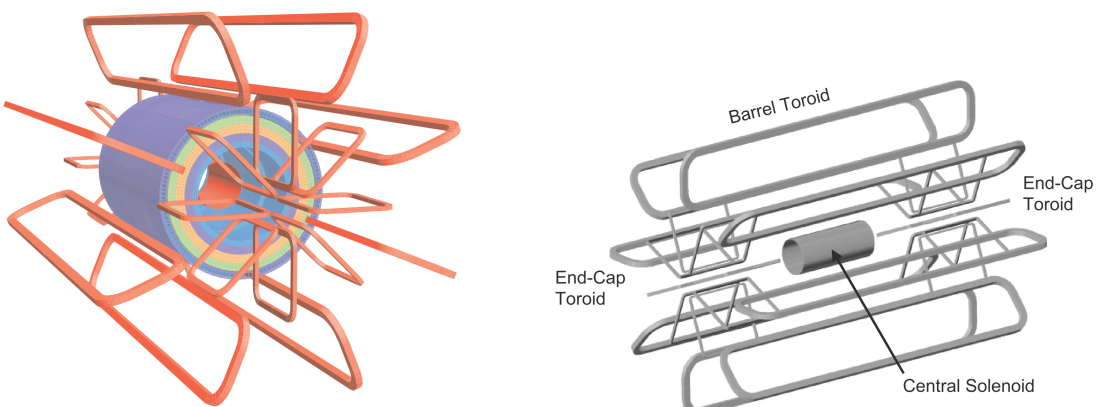
$$\eta \equiv -\ln(\tan(\theta/2))$$

320 Here  $\theta$  is the polar angle. The azimuthal angle,  $\phi$ , is defined around the beam axis and  
321 the polar angle. In the  $(\eta, \phi)$  space a distance  $\Delta R$  can be therefore defined as

$$\Delta R = \sqrt{\Delta\eta^2 + \Delta\phi^2}$$

322 where  $\Delta\eta$  and  $\Delta\phi$  are the differences in pseudorapidity and azimuthal angle between  
323 any two considered objects. A central and a forward region of pseudorapidity are also  
324 defined such that the detector components are described as part of the *barrel* if they belong  
325 to the former or as part of the *end-caps* if they belong to the latter.

326 **2.2.1 The Magnet System**



(a) Geometry of magnet windings and tile calorimeter steel. The eight barrel toroid coils, with the end-cap coils interleaved are visible. The solenoid winding lies inside the calorimeter volume [2].

(b) Schematic view of the superconducting magnets [14].

Figure 2.3: The ATLAS magnet system.

<sup>327</sup> The ATLAS magnet system, 26 m long with a 22 m diameter, generates the magnetic  
<sup>328</sup> field needed to bend the trajectories of charged particles in order to perform momentum  
<sup>329</sup> measurement. Figure 2.3a and 2.3b show the geometry of the system and its compo-  
<sup>330</sup> nents, which are made of NbTi - superconducting material - and will be described in the  
<sup>331</sup> following paragraphs.

### <sup>332</sup> The Central Solenoid

<sup>333</sup> With an axial length of 5.8 m, an inner radius of 2.46 m, and an outer radius of 2.56 m, the  
<sup>334</sup> central solenoid magnet is located between the ID and the ECAL. Its function is to bend  
<sup>335</sup> the charged particles that go through the ID and it is aligned on the beam axis providing  
<sup>336</sup> a 2 T axial magnetic field that allows accurate momentum measurement up to 100 GeV  
<sup>337</sup> [14].

### <sup>338</sup> The Barrel and the End-cap Toroids

<sup>339</sup> Figure 2.3b displays the toroid magnetic system that surrounds the calorimeters. With  
<sup>340</sup> its cylindrical shape this component consists of a barrel and two end-caps toroids, each  
<sup>341</sup> with eight superconducting coils. The system allows accurate measurement of muon  
<sup>342</sup> momenta using a magnetic field of approximately 0.5 T (barrel) for the central regions  
<sup>343</sup> and 1 T (end-cap) for the end-cap regions, respectively, which bends the particles in the  
<sup>344</sup>  $\theta$  direction.

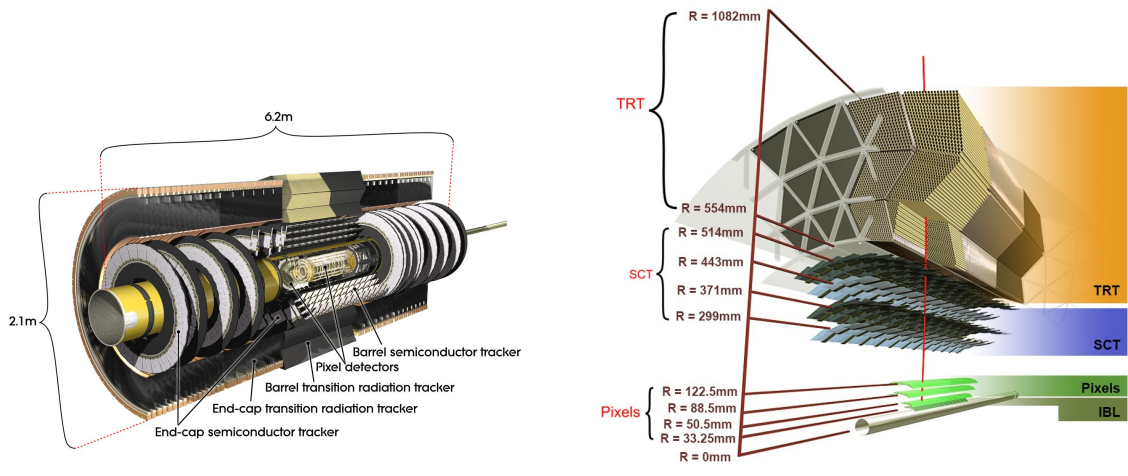
#### <sup>345</sup> 2.2.2 The Inner Detector

<sup>346</sup> The Inner Detector (ID) [15] is the innermost component of the ATLAS detector i. e. the  
<sup>347</sup> nearest sub-detector to the interaction region and it is used to reconstruct charged particle  
<sup>348</sup> tracks used in the selection of physics objects. In fact, it allows robust track reconstruc-  
<sup>349</sup> tion, with accurate impact parameter resolution ( $\sim 20\mu m$ ) and precise primary and sec-  
<sup>350</sup> ondary vertex reconstruction for charged particles (tracks) above 500 MeV and within  
<sup>351</sup>  $|\eta| < 2.5$ .

<sup>352</sup> The ID is comprised of independent and concentric sub-systems, which are all shown  
<sup>353</sup> in Figure 2.4:

- <sup>354</sup> • Insertable B-Layer (IBL):

<sup>355</sup> innermost Pixel Detector layer added during ATLAS Run-2 upgrade (2013/2014)  
<sup>356</sup> to improve vertexing and impact parameter reconstruction;



(a) Overview of the ATLAS ID with labels and dimensions.

(b) Diagram of the ATLAS ID and its sub-detectors.

Figure 2.4: The ATLAS Inner Detector

357     • Silicon Pixel Tracker (Pixel):

358       made of silicon pixel layers and used mainly for reconstructing both the primary  
359       and secondary vertices in an event;

360     • SemiConductor Tracker (SCT):

361       comprised of silicon microstrip layers; thanks to its resolution ( $17 \times 580 \mu\text{m}$ ) it can  
362       accurately measure particle momenta;

363     • Transition Radiation Tracker (TRT):

364       final layer comprised of various layers of gaseous straw tube elements surrounded  
365       by transition radiation material.

366       These sub-detectors will be discussed in the following sections.

367     **IBL**

368       The IBL [16] is the innermost Pixel Detector layer as shown in Figure 2.4b. It is comprised  
369       of 6M channels and each pixel measures  $50 \times 250 \mu\text{m}$ . Its resolution is  $8 \times 40 \mu\text{m}$ . The  
370       addition of this new layer brought a considerable improvement on the performance of the  
371       Pixel Detector by enhancing the quality of impact parameter reconstruction of tracks. In  
372       particular, this was achieved by improving the vertex finding efficiency and the tagging  
373       of bottom-quark-initiated jets ( $b$ -jets) which, in case of a B-layer failure, can be restored  
374       by the IBL. Besides these improvements, the IBL insertion allowed ATLAS to better cope

<sup>375</sup> with high luminosity effects such as the increase in event pile-up, which leads to high  
<sup>376</sup> occupancy and read-out inefficiency.

### <sup>377</sup> **Pixel**

<sup>378</sup> The Pixel detector is comprised of 1750 identical sensorchip-hybrid modules, each cover-  
<sup>379</sup> ing an active area of  $16.4 \times 60.8$  mm. The total number of modules correspond to roughly  
<sup>380</sup> 80 million semiconductor silicon pixels. The nominal pixel size is  $50 \mu\text{m}$  in the  $\phi$  direction  
<sup>381</sup> and  $400 \mu\text{m}$  in the barrel region, along the  $z$ -axis (beam axis) [17]. The reason why such a  
<sup>382</sup> large amount of pixels is employed is justified by the need to cope with the high lumino-  
<sup>383</sup> sity in ATLAS. The silicon pixel detector measures 48.4 cm in diameter and 6.2 m in length  
<sup>384</sup> providing a pseudorapidity coverage of  $|\eta| < 2.5$ . Figure 2.4b shows the three concentric  
<sup>385</sup> barrel layers placed at 50.5 mm, 88.5 mm and 122.5 mm respectively. Furthermore, the  
<sup>386</sup> Pixel detector is made of six disk layers, three for each forward region, such that when a  
<sup>387</sup> charged particle crosses the layers it will generate a signal at least in three space points.  
<sup>388</sup> The fine granularity of such detector allows accurate measurement and precise vertex  
<sup>389</sup> reconstruction, as it provides a more accurate position measurement as a large detection  
<sup>390</sup> area is available. In particular, it has a resolution of  $10 \times 115 \mu\text{m}$ .

### <sup>391</sup> **SCT**

<sup>392</sup> The SCT is made of 4088 modules of silicon micro-strip detectors arranged in four con-  
<sup>393</sup> centric barrel layers. It is mainly used for precise momentum reconstruction over a range  
<sup>394</sup>  $|\eta| < 2.5$  and it was designed for precision measurement of the position using four points  
<sup>395</sup> (corresponding to eight silicon layers), obtained as track hits when crossing the layers.  
<sup>396</sup> Figure 2.4b shows the structure of the SCT with its four concentric barrel layers with  
<sup>397</sup> radii ranging from 299 mm to 514 mm and two end-cap layers. Each module has an in-  
<sup>398</sup> trinsic resolution of  $17 \mu\text{m}$  in the  $R - \phi$  direction and  $580 \mu\text{m}$  in the  $z$  direction. As the  
<sup>399</sup> SCT is further away from the beam-pipe than the Pixel detector, it has to cope with re-  
<sup>400</sup> duced particle density. This allows for reduced granularity maintaining the same level of  
<sup>401</sup> performance of the Pixel detector: SCT can use  $\sim 6.3$  million read-out channels.

### <sup>402</sup> **TRT**

<sup>403</sup> The last and outermost of the sub-systems in the ID is the TRT. It is a gaseous detector  
<sup>404</sup> which consists of 4 mm diameter straw tubes wound from a multilayer film reinforced  
<sup>405</sup> with carbon fibers and containing a  $30 \mu\text{m}$  gold plated tungsten wire in the center. The

straw is filled with a gas mixture of 70% Xe, 27% CO<sub>2</sub> and 3% O<sub>2</sub> [18]. As shown in Figure 2.4b, its section consists of three concentric layers with radii ranging from 544 mm to 1082 mm, each of which has 32 modules containing approximately 50,000 straws, 1.44 m in length, aligned parallel to the beam direction with independent read-out at both ends. Both end-cap sections are divided into 14 wheels, with roughly 320,000 straws in the R-direction. The average 36 hits per track in the central region of the TRT allow continuous tracking to enhance pattern recognition and momentum resolution in the  $|\eta| < 2.5$  region. It also improves the  $p_T$  resolution for longer tracks.

### 2.2.3 The Calorimeters

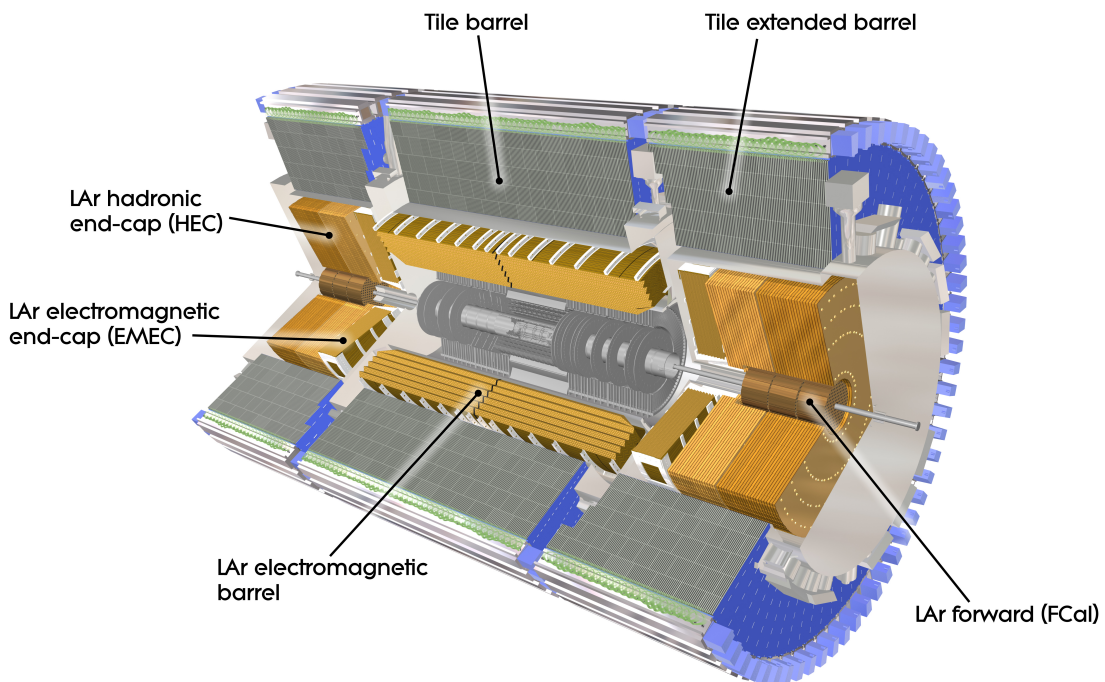


Figure 2.5: A computer generated image of the full calorimeter.

The ATLAS Calorimeter system, shown in Figure 2.5, is comprised of two main subsystems; the electromagnetic calorimeter (ECAL) and hadronic calorimeter (HCAL), which are designed to stop and measure the energy of electromagnetic-interacting and hadronic particles respectively. The combination of the two provides full coverage in  $\phi$  and  $|\eta| < 4.95$ . Particles slow down and lose energy generating showers when crossing different layers. The ECAL is comprised of one barrel and two end-cap sectors employing liquid Argon (LAr). The showers hereby develop as electrons pairs which are then collected. The HCAL is also comprised of one barrel and two end-cap sectors. The sensors

423 in the barrel of the HCAL are tiles of scintillating plastic whereas LAr is employed for  
 424 the end-cap. A forward region, the closest possible to the beam, is covered by a LAr for-  
 425 ward calorimeter (FCal). The LAr and Tile Calorimeter will be briefly discussed in the  
 426 following paragraphs.

## 427 **The Liquid Argon Calorimeters**

428 The ECAL is comprised of multiple layers of liquid Argon (LAr) sampler and lead ab-  
 429 sorber. The choice of its accordion-geometry design brought two main advantages; full  
 430  $\phi$  coverage with no non-interactive regions (no cracks); fast extraction of signals coming  
 431 from both front or rear end of the electrodes. It is made of two half-barrel wheels, both  
 432 placed in the barrel cryostat, that provide a pseudorapidity coverage up to  $|\eta| < 1.475$   
 433 and two end-cap detectors providing  $1.375 \leq |\eta| \leq 3.20$  coverage in two end-cap cryo-  
 434 stats. The junction between the barrel and end cap components defines the crack region  
 435 and any signal coming from the crack region is therefore discarded.

436 In the  $|\eta| < 1.8$  region there is an additional layer, placed at the front of the calori-  
 437 meter, that is made of a thin (0.5 cm in the end-cap and 1.1 cm in the barrel) LAr layer  
 438 with no absorber [19]. This additional layer was designed to correct for the energy lost,  
 439 as particles enter the calorimeter, by taking a measurement just before the majority of the  
 440 electromagnetic shower is developed.

## 441 **The Tile calorimeter**

442 The main purpose of the hadronic calorimeter is to measure the energy of hadronic  
 443 showers. It is built employing steel and scintillating tiles coupled to optical fibres which  
 444 are read out by photo-multipliers. As shown in Figure 2.5, the HCAL is made up of three  
 445 cylinders; a central barrel, 5.64 m long covering a region  $|\eta| < 1.0$ , and two extended  
 446 barrel, 2.91 m long covering a reigon  $0.8 < |\eta| < 1.7$ . Each cylinder is made up of 64  
 447 modules and each module is in turn made up of three layers. Ultimately, the smallest  
 448 section of the calorimeter module is a cell with a  $\Delta\phi \times \Delta\eta = 0.1 \times 0.1$  granularity for the  
 449 two innermost layers and  $\Delta\phi \times \Delta\eta = 0.2 \times 0.1$  for the outermost one.

### 450 **2.2.4 The Muon Spectrometer**

451 The MS [20], shown in Figure 2.6, is the outermost sub-system of the whole ATLAS de-  
 452 tector. As such, it surrounds the calorimeters and its main function is to perform precision

453 measurement of muons momenta. The deflection of muon tracks employing large super-  
 454 conducting air-core toroid magnets and high-precision tracking chambers is at the heart  
 455 of such high precision measurement.

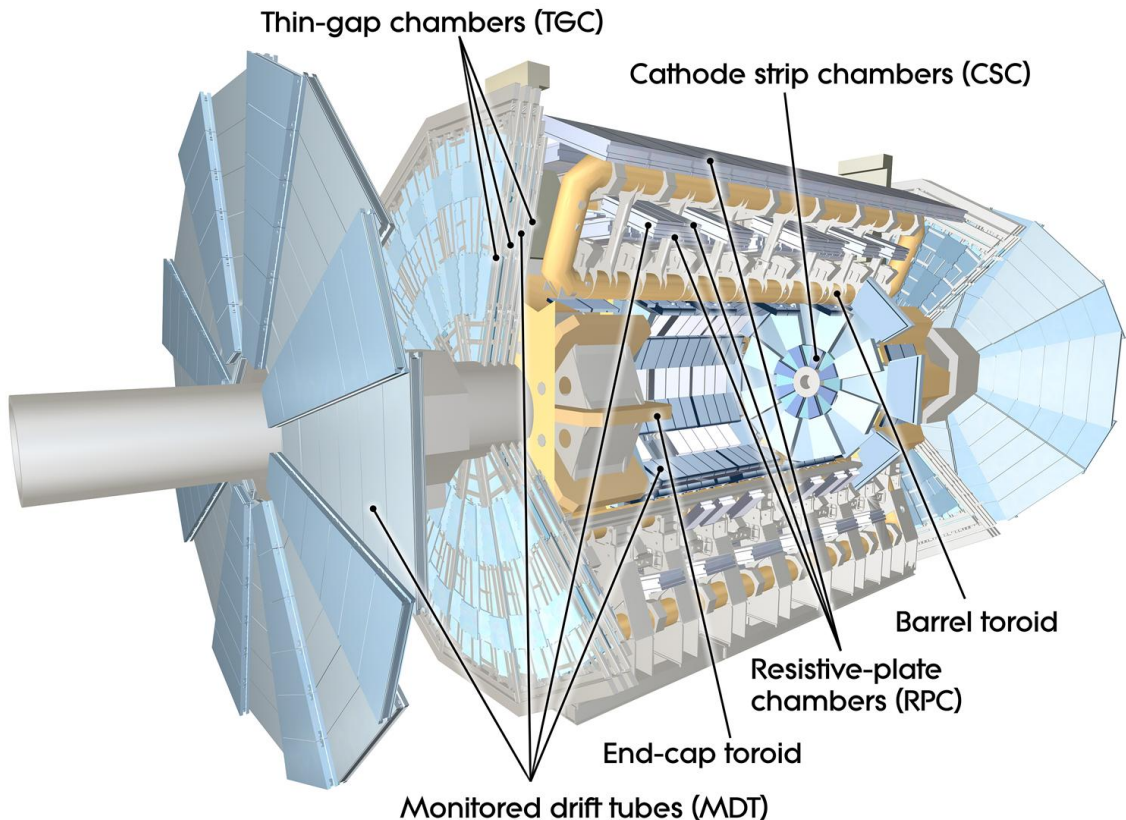


Figure 2.6: Cut-away view of the ATLAS muon system [2].

456 The MS is comprised of one large barrel toroid, covering the region  $|\eta| \leq 1.4$ , and two  
 457 end-cap toroids, covering  $1.6 < |\eta| \leq 2.7$  which are employed together to achieve the  
 458 track-bending effect wanted. The magnitude of the magnetic field in the barrel, generated  
 459 by eight large superconducting coils, ranges from 0.5 to 2 T.

460 Around the beam axis, three cylindrical layers make way for the chambers, placed in  
 461 planes perpendicular to the beam, used to measure tracks.

462 Monitored Drift Chambers (MDTs) are employed over most of the pseudorapidity  
 463 range to provide precision measurement of track coordinates in the bending direction.  
 464 Cathode Strip Chambers (CSCs) are instead employed at large pseudorapidity ( $2 < |\eta| <$   
 465 2.7). Finally, in the end-cap regions Thin-Gap Chambers (TGCs) together with Resistive-  
 466 Plate Chambers (RPCs) are dedicated to the Trigger System discussed in Section 2.3.

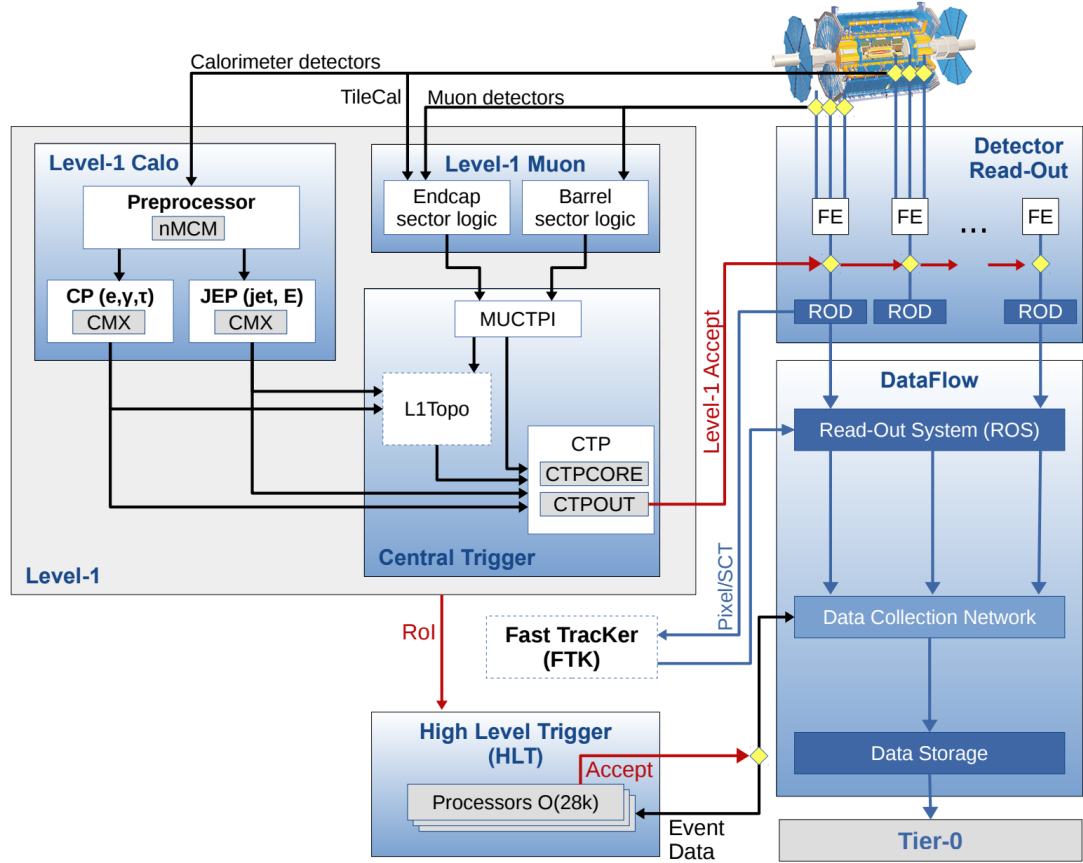


Figure 2.7: The ATLAS TDAQ system. L1Topo and FTK were being commissioned during 2015 and not used for the results shown in this thesis [3].

### 467 2.3 The ATLAS Trigger System

468 The ATLAS Trigger System is at the heart of data taking. It is an essential component of  
 469 any nuclear or particle physics experiment since it is responsible for deciding whether  
 470 or not to store an event for later study [3]. The ATLAS Trigger system is employed to  
 471 reduce the event rate from  $\sim 40$  MHz<sup>1</sup> bunch-crossing<sup>2</sup> to  $\sim 200$  Hz which corresponds  
 472 to roughly 300 MB/s.

473 The Trigger and Data Acquisition (TDAQ) system shown in Figure 2.7 consists of  
 474 a hardware-based first level trigger (L1) and a software-based high-level trigger (HLT).  
 475 The L1 trigger decision is formed by the Central Trigger Processor (CTP), which receives  
 476 inputs from the L1 calorimeter (L1Calo) and L1 muon (L1Muon) triggers. The first level  
 477 (L1), which was designed to perform the first selection step, is a hardware-based system

<sup>1</sup>The LHC delivers beams with a bunch-spacing of 25 ns.

<sup>2</sup>The term bunch-crossing is hereby used when referring to a collision between two bunches of protons.

Since only a certain fraction of the total momentum carried by each proton contributes to the collision, an average number of interactions per bunch-crossing,  $\langle \mu \rangle$  is used.

478 that uses information from the calorimeter and muon subdetectors. It also defines the so-  
 479 called Regions of Interest (RoIs) within the detector to be investigated by the next level  
 480 trigger, the HLT. Additionally, a Fast TracKer (FTK) system [21] (not yet installed) will  
 481 provide global ID track reconstruction at the L1 trigger rate using lookup tables stored  
 482 in custom associative memory chips for the pattern recognition. The FPGA-based track  
 483 fitter will perform a fast linear fit and the tracks are made available to the HLT. This  
 484 system will allow the use of tracks at much higher event rates in the HLT than is currently  
 485 affordable using CPU systems. However, the upgrade of the ATLAS trigger will not be  
 486 discussed any further.

487 In the next sections the L1 and HLT will be briefly described.

### 488 2.3.1 Level 1 Trigger

489 The Level 1 Trigger identifies Regions of Interest (RoIs)<sup>3</sup> and passes these to HLT which  
 490 will perform further investigations. Furthermore, in order to decide whether or not the  
 491 event processing will continue, L1 selection uses only information coming from some  
 492 parts of the detector to keep the input rate to a maximum of 100 kHz. L1 is implemented  
 493 in fast custom electronics to keep the latency<sup>4</sup> below 2.5  $\mu$ s. Event data from other sub-  
 494 syststem are temporarily stored in memories whilst L1 decision is taken.

495 The L1 topological trigger (L1-Topo) [22] is feeded with energy and direction inform-  
 496 ation, about the objects found by the L1 calorimeter and the muon trigger, which will be  
 497 processed by dedicated algorithms implemented in its own FPGAs. However, due to the  
 498 100 kHz read-out rate, not all the information collected by L1-Topo will be sent to the  
 499 HLT, but only part of it. In order to properly seed the ROI-guided HLT reconstruction,  
 500 specific objects in combination with the correct topological criteria must be employed.

### 501 2.3.2 High-Level Trigger

502 The HLT is used to reduce the output rate down to 1 kHz and it has a  $\sim$ 200 ms average  
 503 decision time. Events that pass L1 trigger are then processed by the HLT using finer-  
 504 granularity calorimeter information, precision measurements from the MS and tracking  
 505 information from the ID. The HLT reconstruction can be run within RoIs identified at L1  
 506 or a so-called full-scan on the full detector can be performed. The track reconstruction in  
 507 the Inner Detector is an essential component of the trigger decision in the HLT and it will

---

<sup>3</sup> $\eta - \phi$  regions where event features have been found by the L1 selection process.

<sup>4</sup>Time needed by an electric signal to get to the front-end electronics.

- <sup>508</sup> be discussed more in detail in Chapter 3

509 **Chapter 3**

510 **The  $b$ -jet Trigger Signature in ATLAS**

511 In this chapter the monitor and performance of the bottom-quark-initiated jet ( $b$ -jet) sig-  
512 nature trigger, this being the author’s “technical/qualification task” to become a qualified  
513 member of the experiment, will be discussed. The efficiencies of some of the Run 2  $b$ -jet  
514 triggers were evaluated using  $3.8 \text{ fb}^{-1}$  of  $pp$  collisions data collected in 2015 with 25 ns  
515 bunch-spacing.

516       The qualification task

517 **3.1 Trigger Efficiency**

518 **Chapter 4**

519 **Event Simulation and Reconstruction**

520 bla bla bla

521 **4.1 Event Generation**

522 bla bla

523 **4.1.1 Parton Distribution Functions (PDFs)**

524 bla bla bla

525 **4.1.2 Matrix Element Calculation**

526 bla bla bla

527 **4.1.3 Parton Showers**

528 bla bla bla

529 **4.1.4 Hadronisation**

530 bla bla bla

531 **4.2 Detector Simulation**

532 bla bla bla

<sup>533</sup> **Chapter 5**

<sup>534</sup> **Stop searches in final states with jets  
and missing transverse energy**

<sup>536</sup> **Chapter 6**

<sup>537</sup> **Results and Statistical Interpretations**

<sup>538</sup> Trigger

<sup>539</sup> bla vlas bla

540 

# Bibliography

- 541 [1] C. Lefèvre, *The CERN accelerator complex.*, <http://cds.cern.ch/record/1260465>.  
 542 viii, 10, 11
- 543 [2] ATLAS Collaboration, *The ATLAS experiment at the CERN Large Hadron Collider*,  
 544 Journal of Instrumentation **3** no. 08, (2008) S08003.  
 545 <http://stacks.iop.org/1748-0221/3/i=08/a=S08003>. viii, 12, 18
- 546 [3] A. Collaboration, *Performance of the ATLAS Trigger System in 2015*, Eur. Phys. J. **C77**  
 547 (2017), [arXiv:1611.09661 \[hep-ex\]](https://arxiv.org/abs/hep-ph/1611.09661). viii, 19
- 548 [4] M. Herrero, *The Standard Model.*, <https://arxiv.org/abs/hep-ph/9812242>. 3
- 549 [5] ATLAS Collaboration, *Observation of a New Particle in the Search for the Standard  
 550 Model Higgs Boson with the ATLAS Detector at the LHC*, Phys.Lett. **B716** (2012),  
 551 [arXiv:1207.7214 \[hep-ex\]](https://arxiv.org/abs/hep-ph/1207.7214). 3
- 552 [6] CMS Collaboration, *Observation of a new boson at a mass of 125 GeV with the CMS  
 553 experiment at the LHC*, Phys.Lett. **B716** (2012), [arXiv:1207.7235 \[hep-ex\]](https://arxiv.org/abs/hep-ph/1207.7235). 3
- 554 [7] A. Pich, *The Standard Model of Electroweak Interactions*, [arXiv:1201.0537 \[hep-ph\]](https://arxiv.org/abs/hep-ph/1201.0537).  
 555 5
- 556 [8] K. A. Olive at al. (Particle Data Group), *Review of Particle Physics*, Chin.Phys. C **38**(9)  
 557 (2014). 6
- 558 [9] J.M. Jowett, M. Schaumann, R. Alemany, R. Bruce, M. Giovannozzi, P. Hermes, W.  
 559 Hofle, M. Lamont, T. Mertens, S. Redaelli, J. Uythoven, J. Wenninger, *The 2015  
 560 Heavy-Ion Run of the LHC*,  
 561 <http://accelconf.web.cern.ch/accelconf/ipac2016/papers/tupmw027.pdf>. 9
- 562 [10] O. S. Brüning, P. Collier, P. Lebrun, S. Myers, R. Ostojic, J. Poole and P. Proudlock,  
 563 *LHC Design Report*, <https://cds.cern.ch/record/782076>. 10

- 564 [11] CMS Collaboration, *The CMS experiment at the CERN LHC*, Journal of  
 565 Instrumentation **3** no. 08, (2008) S08004.  
 566 <http://stacks.iop.org/1748-0221/3/i=08/a=S08004>. 10
- 567 [12] LHCb Collaboration, et. al, *The LHCb Detector at the LHC*, JINST (2008). 10
- 568 [13] ALICE Collaboration, *The ALICE experiment at the CERN LHC*, Journal of  
 569 Instrumentation **3** no. 08, (2008) S08002.  
 570 <http://stacks.iop.org/1748-0221/3/i=08/a=S08002>. 10
- 571 [14] A. Yamamoto, Y. Makida, R. Ruber, Y. Doi, T. Haruyama, F. Haug, H. ten Kate,  
 572 M. Kawai, T. Kondo, Y. Kondo, J. Metselaar, S. Mizumaki, G. Olesen, O. Pavlov,  
 573 S. Ravat, E. Sbrissa, K. Tanaka, T. Taylor, and H. Yamaoka, *The ATLAS central*  
 574 *solenoid*, Nuclear Instruments and Methods in Physics Research Section A:  
 575 Accelerators, Spectrometers, Detectors and Associated Equipment **584** no. 1, (2008)  
 576 53 – 74.  
 577 <http://www.sciencedirect.com/science/article/pii/S0168900207020414>. 12,  
 578 13
- 579 [15] ATLAS Collaboration, *The ATLAS Inner Detector commissioning and calibration*, Eur.  
 580 Phys. JC**70**, arXiv:1004.5293. 13
- 581 [16] ATLAS Collaboration, *ATLAS Insertable B-Layer Technical Design Report*,  
 582 <https://cds.cern.ch/record/1291633>. 14
- 583 [17] G. A. et al., *ATLAS pixel detector electronics and sensors*, Journal of Instrumentation **3**  
 584 no. 07, (2008) P07007. <http://stacks.iop.org/1748-0221/3/i=07/a=P07007>. 15
- 585 [18] A. Bingül, *The ATLAS TRT and its Performance at LHC*, Journal of Physics:  
 586 Conference Series **347** no. 1, (2012) 012025.  
 587 <http://iopscience.iop.org/article/10.1088/1742-6596/347/1/012025/meta>.  
 588 16
- 589 [19] ATLAS Collaboration, *ATLAS liquid-argon calorimeter: Technical Design Report*,  
 590 <https://cds.cern.ch/record/331061>. 17
- 591 [20] ATLAS Collaboration, *ATLAS muon spectrometer: Technical design report*,  
 592 <https://cds.cern.ch/record/331068>. 17
- 593 [21] ATLAS Collaboration, *Fast TracKer (FTK) Technical Design Report*,  
 594 <https://cds.cern.ch/record/1552953>. 20

- 
- 595 [22] E. Simoni, *The Topological Processor for the future ATLAS Level-1 Trigger: from design to*  
596 *commissioning*, [arXiv:1406.4316](https://arxiv.org/abs/1406.4316). 20